All-in-one structured textile energy storage electrodes prepared via Janus bond assembly-induced electrodeposition

Seokmin Lee [a], Younji Ko [a], Woojae Chang [a], Cheong Hoon Kwon [b], Younghoon Kim [c,*], Bongjun Yeom [d,*], Jinhan Cho [a,e,*]

[a] Department of Chemical and Biological Engineering, Korea University, Seoul 02841, Republic of Korea
[b] Division of Energy Engineering, Kangwon National University, Samcheok 25913, Republic of Korea
[c] Department of Chemistry, Kookmin University, Seoul 02707, Republic of Korea
[d] Department of Chemical Engineering, Hanyang University, Seoul 04763, Republic of Korea
[e] KU-KIST Graduate School of Converging Science and Technology, Korea University, Seoul 02841, Republic of Korea

ARTICLE INFO

ABSTRACT

One of the most critical issues in developing high-performance textile-based energy storage (TES) electrodes is to effectively incorporate conductive and electrochemically active components into insulating textiles, maintaining the high mechanical flexibility and large surface area of pristine textiles. Herein, we report a high-performance TES electrode prepared from a Janus bond assembly of nonnoble metal-based nanoparticles (NPs) and subsequent electrodeposition. First, tetraoctylammonium-stabilized copper sulfide NPs (TOA-Cu$_x$S NPs) with a diameter of ~10 nm were synthesized in organic media, which were Janus bond layer-by-layer (JB LbL)-assembled with cysteamine (CA) linkers onto cotton textiles. In this case, CA linkers directly and robustly bridged all the interfaces between the OH-functionalized textile and Cu$_x$S NPs as well as between neighboring Cu$_x$S NPs. Additionally, the JB LbL-assembled Cu$_x$S NPs perfectly converted the insulating textile to a conductive textile with a uniform fibril structure and oxidation stability. For the preparation of pseudocapacitive textiles, the subsequent Ni electrodeposition was further carried out onto the conductive and hydrophilic (TOA-Cu$_x$S NP/CA)$_n$ multilayer-coated textile. The formed TES electrodes exhibited a low sheet resistance of 0.03 Ω sq^{-1}, a highly uniform fibril structure, a considerably high areal capacitance of 2.56 F cm^{-2} (at 3 mA cm^{-2}), and high operational stability (i.e., capacity retention of 88.6 % after 10,000 cycles).

1. Introduction

The recent rapid progress and explosive growth of a variety of portable and wearable electronics have strongly stimulated interest in developing high-performance energy storage electrodes with improved energy/power density and mechanical flexibility, reduced mass, and superior operational stability through facile and cost-effective methods [1–8]. Among various energy storage electrodes, a textile-based electrode has been regarded as one of the most ideal electrodes that can sufficiently meet the abovementioned requirements [9–11]. However, given that pristine textile substrates such as natural cotton or silk primarily have insulating properties, electrically conductive components should be preferentially and conformally deposited onto all fibrils from the exterior to the interior of the textile. Additionally, the formed textile electrodes should have relatively low resistance and uniform/robust electrode structure without agglomeration of both conductive components and electrochemically active components for reducing charge transfer resistance within the electrode as well as for increasing active surface area and operational stability [12–14]. These requirements play a pivotal role in determining the overall energy performance of textile energy storage (TES) electrodes.

In line with these needs, conductive textiles have been prepared through various approaches, such as carbonization of textiles [15,16], electroless metal deposition (i.e., chemical reduction of metal ions) onto textiles [17,18], metal complex inks (Ag or Cu complex ink) requiring additional treatments (i.e., thermal, chemical or plasma treatments) [19,20], and physical incorporation of carbon-based materials and/or conducting polymers into textiles [11,21–24]. Furthermore, for the completion of TES electrodes, the electrochemically active components have been additionally deposited onto the formed conductive textiles

---

mainly using the slurry casting method [25].

However, the use of conductive components such as carbon-based materials and/or conducting polymers for the preparation of conductive textiles can induce sluggish electron transfer within electrodes due to their intrinsically low electrical conductivity as well as the high contact resistance occurring from the separation gap between neighboring conductive components [26–28]. Although it has been recently reported that metal nanoparticles (NPs) can prepare conductive textiles through amine-rich organic linker-based layer-by-layer (LbL) assembly, the reported approach has been limited to only noble metal NPs, such as Au or Ag NPs [10,29]. Nevertheless, the resultant conductive textiles prepared from the assembled noble metal NPs still exhibited relatively high electrical resistance ($>0.1 \ \Omega \ sq^{-1}$) compared to bulk metals due to the numerous contact resistances (i.e., the presence of organic ligands bound to the surface of metal NPs and the separation distance between adjacent metal NPs). In addition, considering the economic feasibility, it is desirable that highly conductive textile electrodes should be implemented using cost-effective nonnoble metal NPs.

Furthermore, the poor interfacial interactions between neighboring conductive components as well as between textile and conductive components can also strongly induce the agglomeration and/or nonuniform deposition of conductive and active components onto
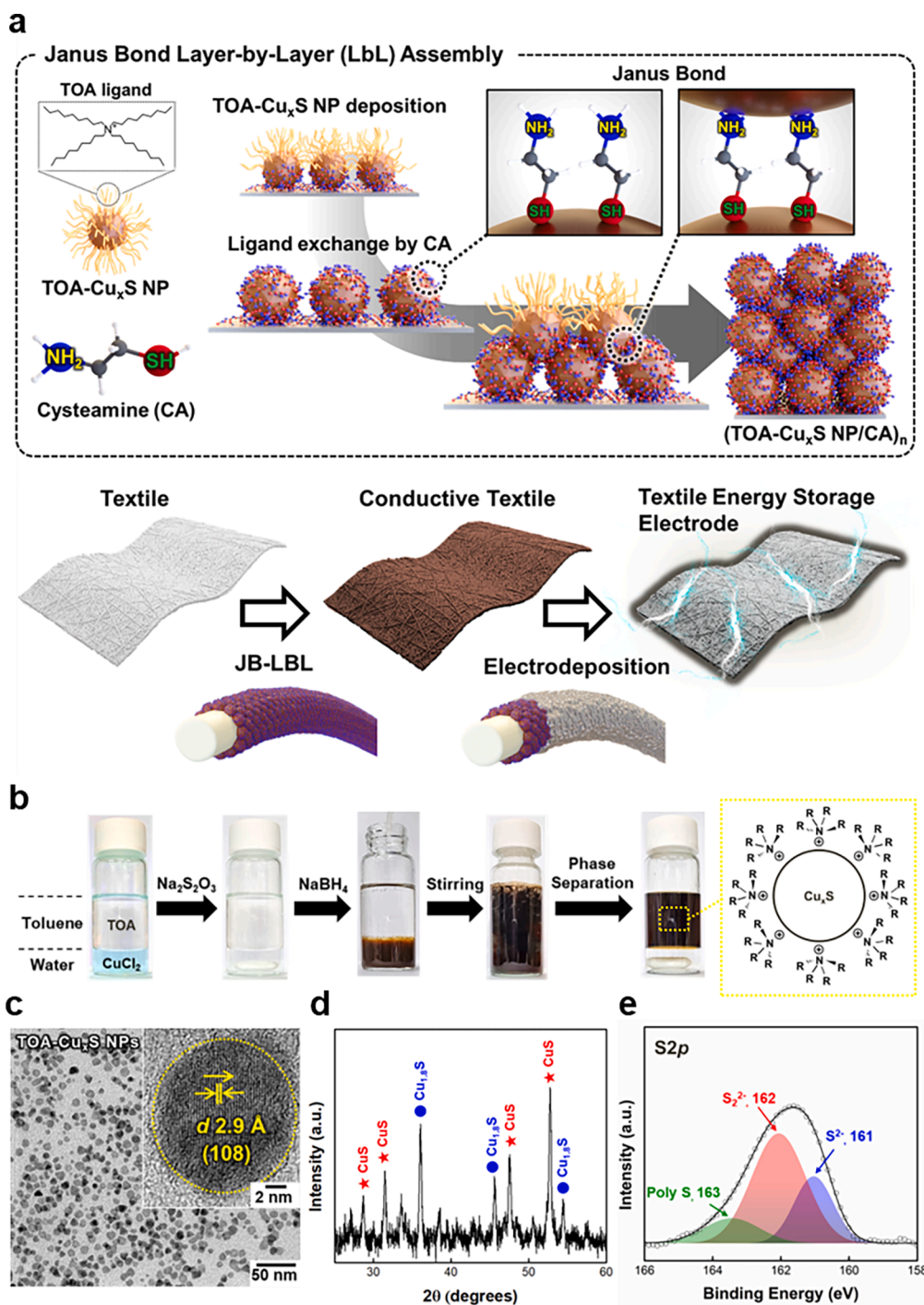

Fig. 1. (a) Metallized textile-type electrochemical electrodes prepared by Janus bond-mediated LbL-assembly of semiconducting copper sulfide (Cu_xS) NPs and electrodeposition. (b) Synthetic process of TOA-Cu_xS NPs dispersed in toluene. (c) HR-TEM images of TOA-Cu_xS NPs. The inset shows that the TOA-Cu_xS NPs have a well-defined crystal structure with a lattice spacing of 2.9 Å (d) XRD pattern of TOA-Cu_xS NPs. (e) XPS spectrum of S2p for the TOA-Cu_xS NPs.

textiles. These undesirable phenomena impose a limit on enhancing the electron transfer/interfacial stability between conductive textile and active components, and furthermore have much difficulty in effectively utilizing the large surface area of textile. As a result, these drawbacks have an adverse effect on the overall performance of electrochemical devices.

Herein, we report a Janus bond-mediated LbL assembly (JB LbL assembly)-induced nickel (Ni) electrodeposition for preparing a high-performance TES electrode with an all-in-one structure, bulk metal-like electrical conductivity, high areal capacitance, good rate capability, and high cycling stability (Fig. 1a). We also demonstrate that nonnoble metal-based Cu_xS NPs can be effectivley LbL-assembled with the NH_2/SH-functionalized organic linkers through their unique adsorption behavior (i.e., JB LbL assembly) and then successfully used as conductive seed components of the insulating textile. Although it has been very recently reported that TES electrode can be prepared using Cu_xS NPs assembly-induced nickel cobalt (NiCo) electrodeposition [30], the LbL-assembly adsorption mechanism between Cu_xS NPs NPs and organic linkers has not been understood, and additionally NiCo layered double hydroxides were used as an electrochemically active layer.

Our research motivation was initiated from the possibilities that NH_2/SH group-containing molecular ligands (i.e., cysteamine, CA) can directly bridge all the interfaces between OH-functionalized textile (i.e., cellulose textile) and Cu_xS NPs as well as between the neighboring Cu_xS NPs. For this study, we synthesized tetraoctylammonium (TOA)-stabilized Cu_xS NPs (TOA-Cu_xS NPs) with semiconducting properties and oxidation-resistant characteristics that have a high affinity with CA linkers containing NH_2 and SH groups in toluene. During LbL assembly of TOA-Cu_xS NPs and CA linkers, the native TOA ligands loosely bound to the surface of Cu_xS NPs could be easily replaced by the SH groups of CA ligands through the ligand exchange reaction. After this process, the unbound, outermost NH_2 groups of the CA linker are successively deposited onto the next adsorbing Cu_xS NPs through an additional ligand exchange reaction between the NH_2 groups and TOA ligands. These alternating bonding moieties formed between the Cu_xS NP and CA ligands during LbL assembly (i.e., JB LbL assembly) could build up the robust multilayers, maintaining the highly porous structure of pristine textile. Particularly, it should be noted that the CA ligand can directly bridge all the interfaces of textiles/Cu_xS NPs and Cu_xS/Cu_xS NPs and significantly minimize the separation distance between neighboring Cu_xS NPs. By increasing the bilayer number (n) of the (TOA-Cu_xS NP/CA)$_n$ multilayers to 10, the sheet resistance of the multilayer-coated textile was significantly decreased to 26 Ω sq^{-1}, and this low sheet resistance value could also be maintained for at least one month.

Based on this JB LbL assembly of Cu_xS NPs and CA ligands, a pseudocapacitive and highly conductive Ni layer could be conformally and robustly electrodeposited onto the LbL-assembled Cu_xS NP layer with hydrophilic and conductive properties. In this case, the Ni-electrodeposited textile (Ni ED-textile) electrodes exhibited an extremely low sheet resistance of ~0.03 Ω sq^{-1} and a high areal capacitance (2.56 F cm^{-2} at 3 mA cm^{-2}) (due to the large active surface area of the electrochemically active Ni layer) and stable operation (i.e., capacity retention of 88.6 % after 10,000 cycles) due to the favorable interfacial interaction and robust all-in-one structure. The full-cell electrode composed of a Ni ED-textile electrode as a cathode and carbonized textile as an anode exhibited high areal capacitances of approximately 1.08 F cm^{-2} at 3 mA cm^{-2}. Given that our pseudocapacitive TES electrodes with high performance and stability can be easily prepared with JB LbL assembly-induced Ni electrodeposition, we believe that our approach can provide a basis for developing a variety of textile-based electrochemical electrodes as well as pseudocapacitive TES electrodes.

2. Experimental section

2.1. Materials

Copper(II) chloride dihydrate (CuCl$_2$·2H$_2$O, ≥99 %), tetra-*n*-octylammonium bromide (TOA, [CH$_3$(CH$_2$)$_7$]$_4$NBr ≥ 98 %). Nickel(II) sulfate hexahydrate (NiSO$_4$·6H$_2$O, ≥98 %), boric acid (H$_3$BO$_3$, ≥99.5 %), and tin(II) chloride dihydrate (SnCl$_2$·2H$_2$O, 98.0 %) were purchased from Alfa Aesar. Sodium thiosulfate (Na$_2$S$_2$O$_3$, 99 %), nickel(II) chloride hexahydrate (NiCl$_2$·6H$_2$O), palladium(II) chloride (PdCl$_2$, 99 %), sodium hypophosphite monohydrate (NaPO$_2$H$_2$·H$_2$O, ≥99 %), ammonium chloride (NH$_4$Cl, ≥99.5 %), sodium citrate dihydrate (Na$_3$C$_6$H$_5$O$_7$·2H$_2$O, ≥99 %), and potassium hydroxide (KOH, 90 %) were purchased from Sigma-Aldrich. Cysteamine (CA, C$_2$H$_7$NS, ≥95 %) and sodium borohydride (NaBH$_4$, ≥98 %) were received from TCI Co. All chemical reagents were used without further purification.

2.2. Synthesis of TOA-Cu_xS NPs

TOA-Cu_xS NPs were synthesized using a modified Brust-Schiffrin method. First, a 25 mM TOA solution in toluene (80 mL) and 33 mM CuCl$_2$·2H$_2$O solution in deionized water (30 mL) were prepared. Then, 12 mmol of Na$_2$S$_2$O$_3$ was added to the CuCl$_2$·2H$_2$O solution and stirred until the solution was clear and transparent. The TOA solution was subsequently added to the abovementioned aqueous solution and stirred vigorously for 15 min at 25 °C. Subsequently, 0.9 M aqueous solution of NaBH$_4$ (10 mL) was further added to the mixture for reduction. After 2 h, the aqueous and toluene phases were clearly separated, and the aqueous phase was subsequently removed. The toluene phase with a dark brown color was washed several times with 10 m$_M$ HCl, 10 m$_M$ NH$_4$OH, and deionized water.

2.3. Janus bond-mediated layer-by-layer assembly of (TOA-Cu_xS NP/CA)$_n$ multilayers

First, the substrates (SiO$_2$-wafers or QCM electrodes) were treated with a UV ozone cleaner before LbL assembly and then dipped into the CA solution (2 mg/ml) for 30 min. After the dipping process, the CA-coated substrate was washed with pure ethanol to remove the weakly adsorbed CA molecules. Subsequently, the CA-coated substrate was immersed into the hydrophobic TOA-Cu_xS NP solution for 30 min and then washed with pure toluene again. These procedures were repeated to form multilayers with the desired thickness or bilayer number (n) (i.e., (TOA-Cu_xS/CA)$_n$ multilayers).

2.4. Preparation of the Ni ED-textile

The as-prepared (TOA-Cu_xS/CA)$_4$ coated-textile was immersed in electroplating solution (Watts bath) (specifically 240 g/L NiSO$_4$·6H$_2$O, 45 g/L NiCl$_2$·6H$_2$O, and 30 g/L H$_3$BO$_3$ were dissolved in deionized water) [31]. Ni was electroplated onto the (TOA-Cu_xS/CA)$_4$-coated textile using a two-electrode system in electroplating solution. In this case, the (TOA-Cu_xS/CA)$_4$-coated textile and the Ni plate were used as a cathode and an anode, respectively. Then, an external current density of 250 mA cm^{-2} was applied to the sample for 10 min at room temperature, and the electroplated sample was washed in deionized water and dried at room temperature.

2.5. Preparation of chemically reduced Ni-textile

Chemical reduction of Ni ions onto the bare textile was carried out using a previously reported procedure [17]. Briefly, cotton textile was first immersed into SnCl$_2$ aqueous solution (0.05 M SnCl$_2$·2H$_2$O and 0.15 M HCl) for 10 min. Then, the substrate was activated in PdCl$_2$ solution (0.6 × 10^{-3} M PdCl$_2$ and 0.03 M HCl). Subsequently, Ni ions were chemically reduced to the Ni layer in the water bath (45 g/L

$NiSO_4 \cdot 6H_2O$, 240 g/L $NaH_2PO_2 \cdot H_2O$, 30 g/L $NaC_6H_5O_7 \cdot 2H_2O$ and 50 g/L NH_4Cl) at 80 °C for 120 min. After the reaction, the chemically reduced Ni textile was repeatedly washed with deionized water and then air dried.

2.6. Preparation of the asymmetric supercapacitor

Ni ED-textile and carbonized textiles were employed as the positive and negative electrodes for asymmetric full-cell pseudocapacitors, respectively. The area ratio of the cathode and anode was adjusted based on the following charge balance equation [32]:

$$q = C \times \Delta E \times S \tag{1}$$

$$\frac{S^+}{S^-} = \frac{C^- \Delta E^-}{C^+ \Delta E^+} \tag{2}$$

where q, C, ΔE, and S refer to the stored charge, areal capacitance (F cm^{-2}), potential window (V) during the CV or GCD operation, and area (cm^2) of the electrodes, respectively.

2.7. Characterization

High-resolution transmission electron microscopy (HR-TEM) of synthesized TOA-Cu_xS NPs was conducted using a Tecnai20 microscope (FEI). The UV–vis absorbance spectra of TOA-Cu_xS NP solution were recorded using a Cary 5000 (Agilent Technologies) within a wavelength window ranging from 400 to 1600 nm. X-ray diffraction (XRD) patterns were obtained using a SmartLab instrument (Rigaku) with Cu Kα radiation. X-ray photoelectron spectroscopy (XPS) analysis was performed by X-TOOL (ULVAC-PHI) with monochromatic Al Kα radiation as the excitation source.

Fourier transform infrared (FTIR) spectra of the multilayers were collected using a CARY 600 spectrometer (Agilent Technology) in Advanced Grazing Angle (AGA) mode with a resolution of 4 cm^{-1}, and the obtained data were plotted using spectrum analysis software (OMNIC, Nicolet). The water contact angle was measured by a sessile drop method using a Phoenix-300 instrument (SEO Corp.) equipped with a video capture camera.

The multilayer film growth was quantitatively monitored using a QCM (QCM 200, SRS). The resonance frequency of the QCM electrodes was approximately 5 MHz. The adsorbed mass of dendrimer and hydrophobic NPs, Δm, was calculated from the change in QCM frequency, ΔF, using the Sauerbrey equation:

$$\Delta F(Hz) = -\frac{2F_0^2}{A\sqrt{\rho_q \mu_q}} \cdot \Delta m \tag{3}$$

where F_0 (~5 MHz) is the fundamental resonance frequency of the crystal; A is the electrode area; and ρ_q (~2.65 g·cm^{-2}) and μ_q (~2.95 × 10^{11} g·cm^{-2}·s^{-2}) are the shear modulus and density of quartz, respectively. This equation can be simplified as follows: [33]

$$\Delta F\ (Hz) = -56.6 \times \Delta m_A \tag{4}$$

where Δm_A is the mass change per quartz crystal unit area in μg·cm^{-2}.

FE-SEM and EDS were conducted using a Quanta 250 FEG (FEI). The surface morphology of the formed multilayers was scanned using atomic force microscopy (AFM, XE-100, Park systems) in tapping mode. The sheet resistance was measured using a four-probe measurement method with a Loresta-GP MCP-T610 (Mitsubishi Chemical Analytech). The current (log I)–voltage (V) profiles of (TOA-Cu_xS/CA)$_n$ multilayers were recorded by a two-probe method using a semiconductor parametric analyzer (Agilent 4155B, Agilent Technologies), and gold wires with a diameter of 0.5 mm were used as the top/bottom electrodes. The temperature dependence of the electrical conductivity of the formed multilayers was measured using a physical property measurement system

(PPMS-9, Quantum Design) over a temperature range from 2 to 300 K. The specific surface area was measured by mercury intrusion porosimetry and could be detected from macropores to mesopores. The experiments were carried out with a Micromeritics instrument (MicroActive AutoPore V9600), which operates over the interval of 0.20 ~ 33 000 psi to estimate the pores between 0.006 and 800 μm.

2.8. Electrochemical measurements

The electrochemical characteristics of textile electrodes were investigated using an Ivium-*n*-Stat (Ivium Technologies). In the three-electrode configuration used to characterize the single electrodes, a Pt wire, a Hg/HgO (saturated by 1 M NaOH), and the textile electrode (active area ~ 1.0 × 1.0 cm^2) were used as the counter, reference, and working electrodes in 6 M KOH electrolyte, respectively. EIS measurements were performed over a frequency range of 100 kHz to 0.1 Hz with a perturbation amplitude of 0.01 V. The electrochemical capacitance values of the textile electrodes were calculated from the GCD discharge profiles according to the following equation [34]:

$$C = \frac{I\Delta t}{S\Delta V} \tag{5}$$

where I, Δt, and ΔV refer to the applied current (A), discharging time (s), and operating potential window (V), respectively. The variable S indicates the area (cm^2) or mass (g) of the active material. The mass of the active material was measured using a previously reported procedure [35]. The Ni ED-textile was immersed in 10 M NH_4OH solution for 24 h at room temperature to selectively remove nickel oxides, including Ni $(OH)_2$ and NiO. In this case, the masses of $Ni(OH)_2$ and NiO were evaluated from the mass difference before and after immersion, and the mass of the resultant nickel oxides was measured to be approximately 3.54 mg cm^{-2}.

3. Results and discussion

3.1. Synthesis of TOA-stabilized Cu_xS NPs dispersed in organic media

For the preparation of Cu_xS NP-based conductive textiles, concentrated TOA-Cu_xS NPs were first synthesized using a modified Brust-Schiffrin method. As shown in Fig. 1b, the Cu_xS NPs synthesized in the aqueous phase were rapidly transferred to the TOA ligand-containing toluene phase, resulting in the formation of TOA-Cu_xS NPs with a diameter of approximately 10 nm that could be highly dispersed in toluene (Fig. 1c). However, in the case of preparing water-dispersible Cu_xS NPs using sodium thiosulfate ($Na_2S_2O_3$) and a reducing agent ($NaBH_4$) in only the aqueous phase, the formed Cu_xS NPs easily aggregated, showing poor dispersion in water, which was in stark contrast to the TOA-Cu_xS NPs prepared from the two-phase system (Fig. S1). These TOA-Cu_xS NPs exhibited broad absorption in the visible and near-infrared regions (by localized surface plasmon resonance) of the electromagnetic spectrum due to their relatively large size distribution (Fig. S2). The crystal structure and chemical state of TOA-Cu_xS NPs were also analyzed by X-ray diffraction (XRD) and X-ray photoelectron spectroscopy (XPS) (Fig. 1d and e), which confirmed that the TOA-Cu_xS NPs were composed of $Cu_{1.8}S$ (digenite) and CuS (covellite) [36]. As shown in Fig. 1e, the S $2p$ spectrum can be deconvoluted into a mono-sulfide (S^{2-}) peak with a binding energy of 161 eV, a disulfide (S_2^{2-}) peak with a binding energy of 162 eV, and a polysulfide (i.e., sulfur in the thiosulfate composition) peak with a binding energy of 163 eV [37]. These results evidently demonstrated that highly concentrated and dispersible Cu_xS NPs could be easily synthesized using TOA ligands in nonpolar media. Furthermore, it was anticipated that the TOA ligands loosely bound to the surface of Cu_xS NPs would be easily replaced by the other organic ligands having a higher affinity for Cu_xS NPs.

3.2. Adsorption behavior of Janus bond-mediated LbL assembly

To confirm the abovementioned possibility, we investigated the ligand exchange reaction between TOA ligands and CA ligands containing NH_2 and SH groups. In this case, the bulky TOA ligands of Cu_xS NPs were almost perfectly replaced by the –NH_2 and -SH groups of small CA ligands without dissolution of Cu_xS NPs, which was mainly due to the higher affinity of Cu_xS NPs for the –NH_2 or -SH groups (Fig. 2a).

Considering that bulky organic ligands of conductive NPs act as insulating barriers, this facile replacement by small molecule ligands can significantly reduce the numerous contact resistances occurring at the interfaces between neighboring Cu_xS NPs.

To this end, the ligand replacement reaction using CA ligands was examined using Fourier transform infrared (FTIR) spectroscopy (Fig. 2b). The FTIR spectra of TOA ligands displayed strong absorption peaks originating from the C—H stretching of bulky/long alkyl chains at
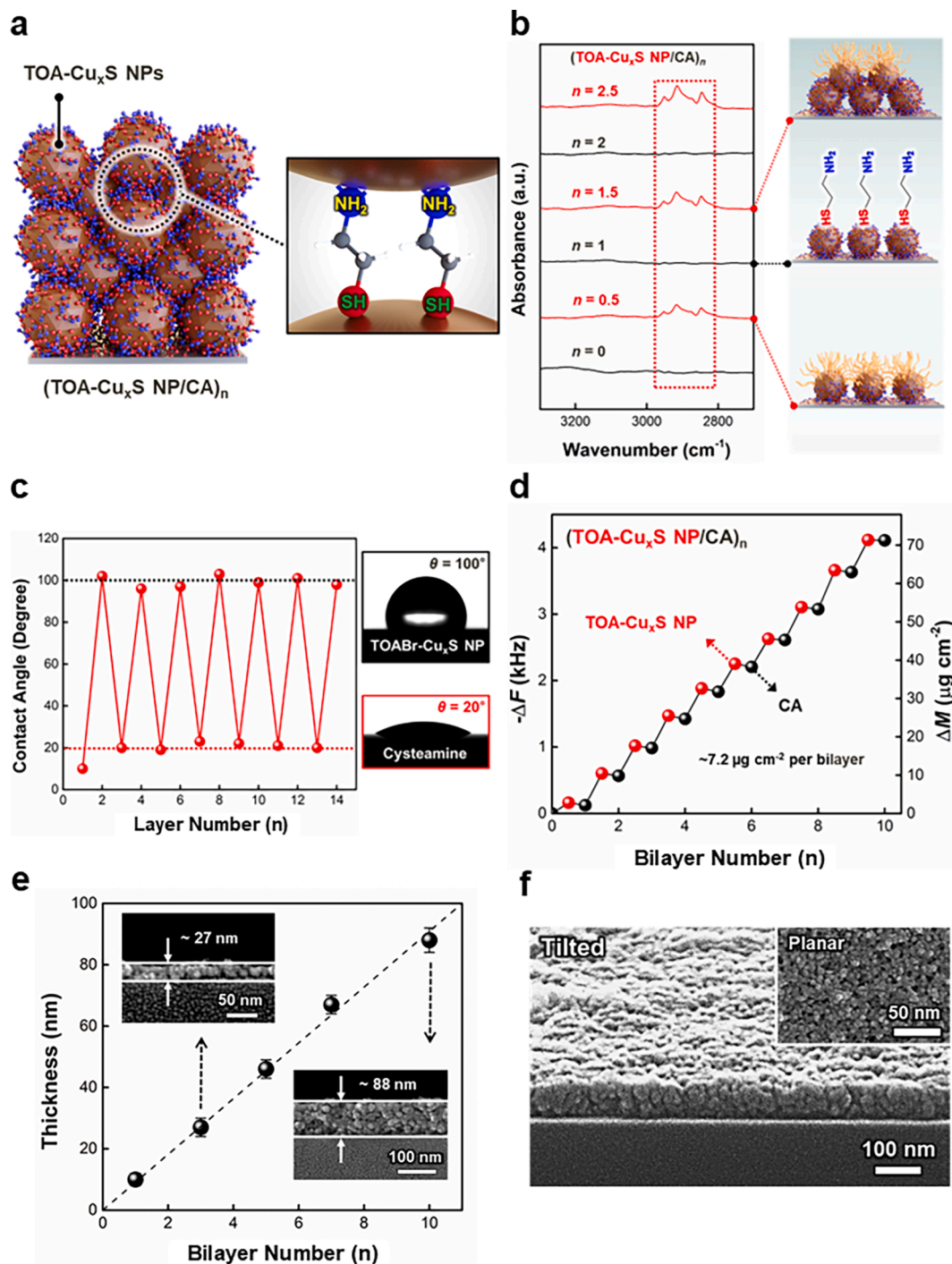

Fig. 2. (a) Schematic illustration of the formation of (TOA-Cu_xS/CA)$_n$ multilayers during JB-mediated ligand replacement LbL assembly. (b) FTIR spectra and schematic representation of JB LbL-assembled (TOA-Cu_xS/CA)$_n$ multilayers as a function of bilayer number (n). (c) Water contact angle test of the JB LbL-assembled Cu_xS NP multilayers. (d) Frequency ($-\Delta F$, left axis) and mass change (Δm, right axis) of (TOA-Cu_xS NP/CA)$_n$ multilayers with increasing bilayer number obtained from QCM analysis. (e) Thickness change of (TOA-Cu_xS NP/CA)$_n$ multilayers on Si wafers as a function of the bilayer number (n), measured from the cross-sectional FE-SEM images (inset). (f) Tilted FE-SEM image of (TOA-Cu_xS NP/CA)$_{10}$ multilayers, and the inset shows a planar FE-SEM image.

2700–3000 cm^{-1}. Therefore, the strong C—H stretching peaks of TOA ligands were traced to confirm the ligand replacement reaction. First, when TOA-Cu$_x$S NPs were LbL-assembled onto the CA-coated substrate, two noticeable absorption peaks derived from the C—H stretching of the outermost TOA ligands bound to the surface of Cu$_x$S NPs were observed in the TOA-Cu$_x$S NP-coated film (i.e., n = 0.5). As the CA layer was further LbL-assembled onto the TOA-Cu$_x$S NP-coated film (i.e., n = 1), the absorption peak intensity of the C—H stretching peaks at 2700–3000 cm^{-1} was significantly decreased. The alternating deposition of the TOA-Cu$_x$S NP array and the CA layer produced inversely correlated changes in the peak intensities of the C—H stretching frequencies. As a result, the Cu$_x$S NP layers (*e.g.,* n = 1.0 and 2.0 bilayered films) sandwiched between adjacent CA layers did not contain the TOA ligands.

We also investigated the adsorption behavior of CA ligands onto the TOA-Cu$_x$S NP layer. If the SH groups of CA are preferentially adsorbed onto the TOA-Cu$_x$S NP layer, it is reasonable to conclude that the outermost functional groups of the CA-coated TOA-Cu$_x$S NP layer are mostly NH$_2$ groups. To confirm this possibility, carboxylic acid (COOH) group-functionalized poly(acrylic acid) (PAA) was deposited on the outermost CA-coated substrate (Fig. S3). This adsorption behavior was also examined by quartz crystal microbalance (QCM) measurements, and the mass changes (Δm) could be quantitatively calculated from the frequency changes (-ΔF) of components adsorbed on the QCM electrodes. When the PAA layer was deposited onto the outermost CA layer-coated QCM electrode, the mass change was increased, implying the formation of stable hydrogen bonding between the COOH groups of PAA and the NH$_2$ groups of CA. As a result, the SH groups of CA ligands were preferentially deposited onto the outermost TOA-Cu$_x$S NP-coated substrate, and therefore, the outermost, residual NH$_2$ groups of CA could induce the adsorption of the next TOA-Cu$_x$S NP layer. These phenomena clearly suggest that TOA-Cu$_x$S NPs and CA ligands could be robustly connected through JB LbL-assembly behavior.

Furthermore, the alternating LbL deposition between hydrophobic TOA-Cu$_x$S NPs and hydrophilic CA ligands generated dramatic changes in the surface wettability measured from the water contact angle test (Fig. 2c). When the CA ligands were deposited onto the Au-sputtered substrate with a high affinity for SH groups, the water contact angle was measured to be approximately 20° due to the hydrophilic property of the outermost NH$_2$ moieties. However, when the TOA-Cu$_x$S NPs were subsequently deposited onto the CA layer-coated substrate, the outermost layer was changed from CA to TOA ligands. In this case, the water contact angle was significantly increased up to approximately 100° because of the hydrophobic property originating from bulky aliphatic chains of TOA ligands. After subsequently depositing the CA ligands onto the TOA-Cu$_x$S NP-coated substrate, the water contact angle was reduced again to approximately 20° due to the outermost hydrophilic NH$_2$ moieties. That is, these dramatic changes in the water contact angles periodically occurred according to the change in the outermost layer. Additionally, given that the surface wettability of the sequentially adsorbed organic and/or NP layers is highly sensitive to the chemical and physical properties of the adsorbed components [38], the periodic oscillation of water contact angles implied that the sufficient surface coverage of the outermost layer could screen the chemical and physical properties of the previously adsorbed layer. Therefore, we envision that when pseudocapacitive electroplating is applied to the conductive textile in aqueous electrolyte solution, the hydrophilicity of the outermost CA layer-coated conductive textile will induce the formation of a highly uniform pseudocapacitive layer on all the fibrils within the conductive textiles.

Based on these results, the adsorbed amounts of (TOA-Cu$_x$S NP/CA)$_n$ multilayers were quantitatively measured from QCM. In the case of consecutively depositing TOA-Cu$_x$S NPs and CA ligands, the regular and vertical growth of (TOA-Cu$_x$S NP/CA)$_n$ multilayers was observed, as shown in Fig. 2d. The deposition of TOA-Cu$_x$S NP and CA ligand generated –ΔF of 0.41 ± 0.04 kHz (Δm of ~7.2 μg·cm^{-2}) per bilayer. A

slight decrease in Δm during the deposition of CA ligands suggested that bulky TOA ligands loosely bound to the surface of the Cu$_x$S NPs were replaced by relatively small CA ligand molecules. Furthermore, despite performing LbL assembly in organic media, it should be noted that NH$_2$-rich organic ligands such as PEI and TREN cannot be LbL assembled with Cu-based nanomaterials, including TOA-Cu$_x$S NPs, because these NPs were easily dissolved by the formation of strong complexation between Cu ions and NH$_2$-rich ligands during LbL assembly (Fig. S4) [39,40].

The total film thicknesses of (TOA-Cu$_x$S NP/CA)$_n$ multilayers were also investigated using cross-sectional field-emission scanning electron microscopy (FE-SEM) (Fig. 2e and f). With increasing bilayer number (n) from 1 to 10, the total thicknesses of the multilayers increased from approximately 9 to 88 nm. Particularly, considering that the CA ligand is an extremely small organic molecule (M$_w$ ~ 77 g mol^{-1}) and that the average diameter of TOA-Cu$_x$S NPs was approximately 10 nm, these results indicated that the LbL-assembled TOA-Cu$_x$S NPs were densely packed in the respective layers, as mentioned earlier. Additionally, atomic force microscopy (AFM) topographic images of the (TOA-Cu$_x$S NP/CA)$_{10}$ multilayers displayed a smooth surface with an areal root-mean-square (rms) roughness of 4.39 nm (Fig. S5). Furthermore, we confirmed that our approach could be easily applied to various substrates, including colloidal particles (Figs. S6 and S7).

3.3. Electrical properties of (TOA-Cu$_x$S NP/CA)$_n$ multilayers

As mentioned earlier, bulky TOA ligands loosely bound to the surface of Cu$_x$S NPs are exchanged by small CA ligands, which can have a significant effect on charge transport between neighboring Cu$_x$S NPs due to the removal of bulky insulating ligands as well as the reduced interparticle distance [41,42]. To investigate the electrical properties of the (TOA-Cu$_x$S NP/CA)$_n$ multilayer, the sheet resistance of multilayers on the flat SiO$_2$ wafer was first measured as a function of bilayer number (n) (Fig. 3a). When the bilayer number was increased up to 10, the sheet resistance and electrical conductivity of the (TOA-Cu$_x$S NP/CA)$_n$ multilayer reached approximately 532 Ω sq^{-1} and 214 S cm^{-1}, respectively, without any additional percolation treatment, such as thermal treatment. Furthermore, the current response level of the (TOA-Cu$_x$S NP/CA)$_n$ multilayers was measured using a two-probe method, which was also compared with that of a spin-coated TOA-Cu$_x$S NP film onto a Si wafer (Fig. 3b). In the case of the spin-coated TOA-Cu$_x$S NP film, its current level was measured to be approximately 1.2×10^{-8} mA (at ±3 V), implying low electrical conductivity, whereas the (TOA-Cu$_x$S NP/CA)$_{10}$ multilayers exhibited a significantly high current level of ~10^{-2} mA. Moreover, as shown in Fig. 3c, all the (TOA-Cu$_x$S NP/CA)$_{n=3, 5, 7, and 10}$ multilayers followed the conduction mechanism relation of $J \propto E^{\alpha}$ ($\alpha \approx 1.0$ for ohmic law), where J is the current density and E is the electric field. These results implied that JB LbL assembly could substantially enhance the charge transport between neighboring Cu$_x$S NPs as a consequence of the reduced contact resistance and interparticle distance.

To better understand the conduction mechanism of (TOA-Cu$_x$S NP/CA)$_n$ multilayers, we further investigated the temperature-dependent electrical resistivity (ρ) of the (TOA-Cu$_x$S NP/CA)$_{10}$ multilayers (Fig. 3d). In this case, the (TOA-Cu$_x$S NP/CA)$_{10}$ multilayers showed semiconducting behavior with temperature-dependent electrical transport mechanisms. In the temperature window ranging from 300 to 238 K, the dominant conduction mechanism was thermally activated band conduction (TAC). On the other hand, in the temperature region ranging from 160 to 115 K, the conduction mechanism of nearest neighbor hopping (NNH) was exhibited. The TAC and NNH conducting regimes could also be expressed with linear dependence (as a plot of ln(ρ) vs T^{-1}), as shown in the following equation [43,44]:

$$\rho(T) = \rho_0 \exp(\Delta E / k_B T) \tag{6}$$

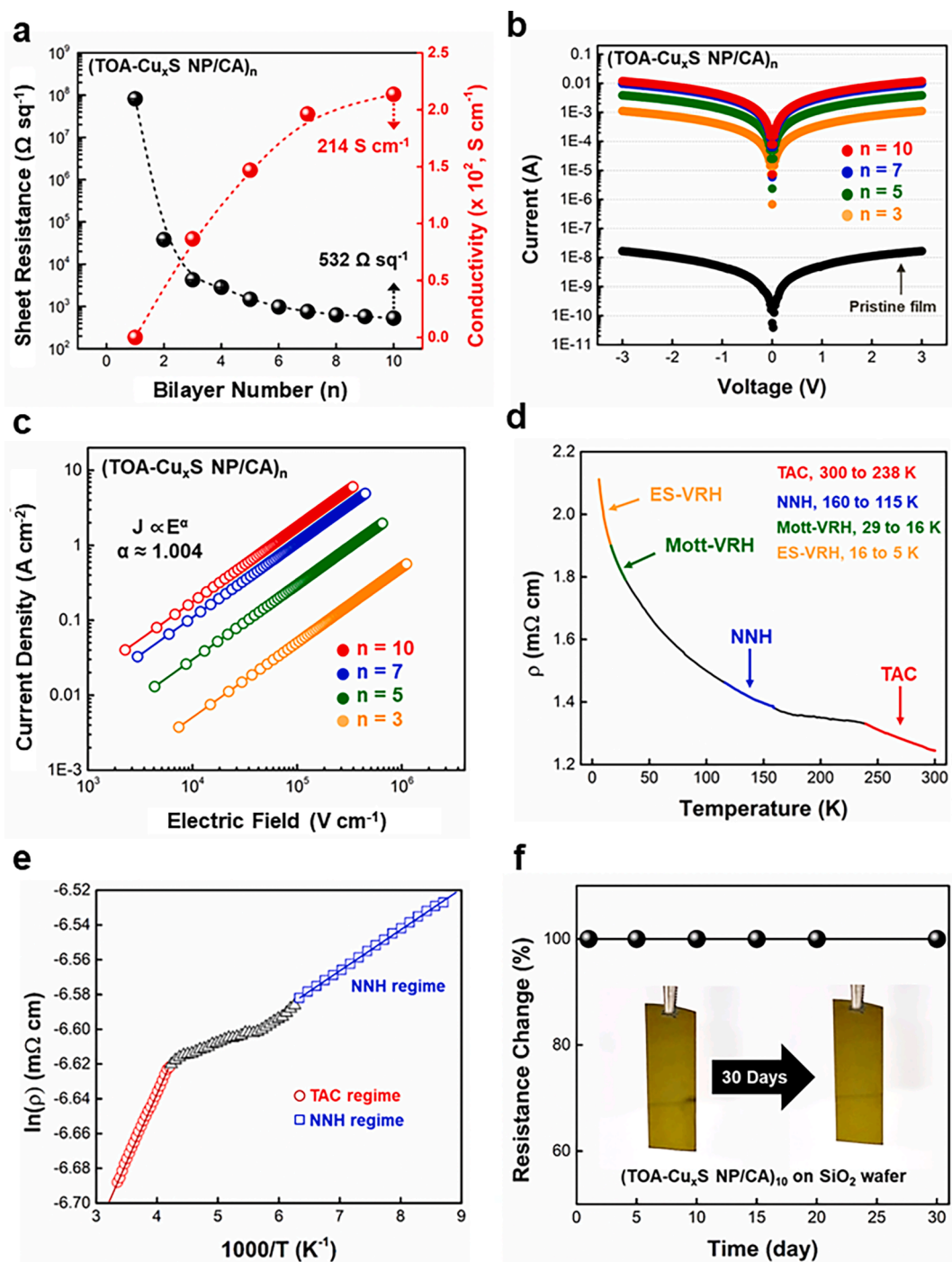where ρ_0, ΔE, k_B, and T refer to a constant, activation energy, Boltz-

Fig. 3. (a) Sheet resistance and electrical conductivity of (TOA-Cu$_x$S NP/CA)$_n$ multilayers on Si wafers as a function of bilayer number. (b) Current (I)–voltage (V) curves, and (c) current density (J)–electric field (E) profiles of (TOA-Cu$_x$S NP/CA)$_n$ multilayers (n = 3, 5, 7, 10). (d) Physical property measurement over a temperature range from 5 to 300 K of (TOA-Cu$_x$S NP/CA)$_{10}$ multilayers. (e) Electrical conduction behavior of (TOA-Cu$_x$S NP/CA)$_{10}$ in the TAC and NNH regime. (f) Electrical stability of (TOA-Cu$_x$S NP/CA)$_{10}$ multilayers under ambient conditions.

mann's constant, and temperature, respectively (Fig. 3e). Additionally, Mott's and Efros-Shklovskii's (ES) mechanisms, as two different types of conduction mechanisms in variable range hopping (VRH), were observed in the lower temperature regime (>30 K) (Fig. S8). These results implied that the intrinsic semiconducting property of Cu$_x$S NPs governs the electron transport mechanism of the (TOA-Cu$_x$S NP/CA)$_{10}$ multilayer film. Furthermore, the electrical conductivity (or electrical resistance) of the (TOA-Cu$_x$S NP/CA)$_{10}$ multilayer could maintain its electrical properties over 30 days in ambient air owing to the strong oxidation-resistant property of Cu$_x$S NPs (Fig. 3f). On the other hand,

conventional Cu NPs stabilized by oleic acid (OA) and/or oleylamine (OAm) ligands have difficulty exhibiting and maintaining the high electrical conductivity of Cu due to their facile oxidation in air and long alkyl chain ligands (i.e., OA/OAm ligands) [45–48].

3.4. Preparation of conductive textile based on (TOA-Cu$_x$S NP/CA)$_n$ multilayers

Based on the unique adsorption behavior (i.e., JB LbL assembly) and electrical properties of (TOA-Cu$_x$S NP/CA)$_n$ multilayers, we tried to

prepare conductive textiles. To this end, CA ligands were first assembled onto OH-functionalized cotton textiles composed of numerous cellulose fibrils using hydrogen-bonding interactions between the NH_2 groups of CA and the OH groups of cellulose fibrils. After this surface modification, the $(TOA-Cu_xS\ NP/CA)_n$ multilayers were consecutively deposited onto 900 μm-thick cotton textiles. In this case, the Cu_xS NPs were uniformly and densely coated onto all the regions ranging from the exterior to the interior of textiles, which was confirmed by FE-SEM and energy dispersive X-ray spectroscopy (EDS) mapping images (Fig. 4a).

Particularly, with increasing bilayer number (n) of $(TOA-Cu_xS\ NP/CA)_n$ multilayers from 1 to 10, the sheet resistance of textiles decreased from approximately 760 to 26 $\Omega\ sq^{-1}$, whereas its electrical conductivity increased from approximately 0.2 to 43 S m^{-1} (including textile thickness) (Fig. 4b). It should be noted that the sheet resistance of $(TOA-Cu_xS\ NP/CA)_{10}$ multilayer-coated textile (26 $\Omega\ sq^{-1}$) was lower than that of $(TOA-Cu_xS\ NP/CA)_{10}$ multilayer on the flat SiO_2 wafer (532 $\Omega\ sq^{-1}$) owing to the interconnected fibril structure which provides numerous electrically conductive pathway within the textile. On the basis of these
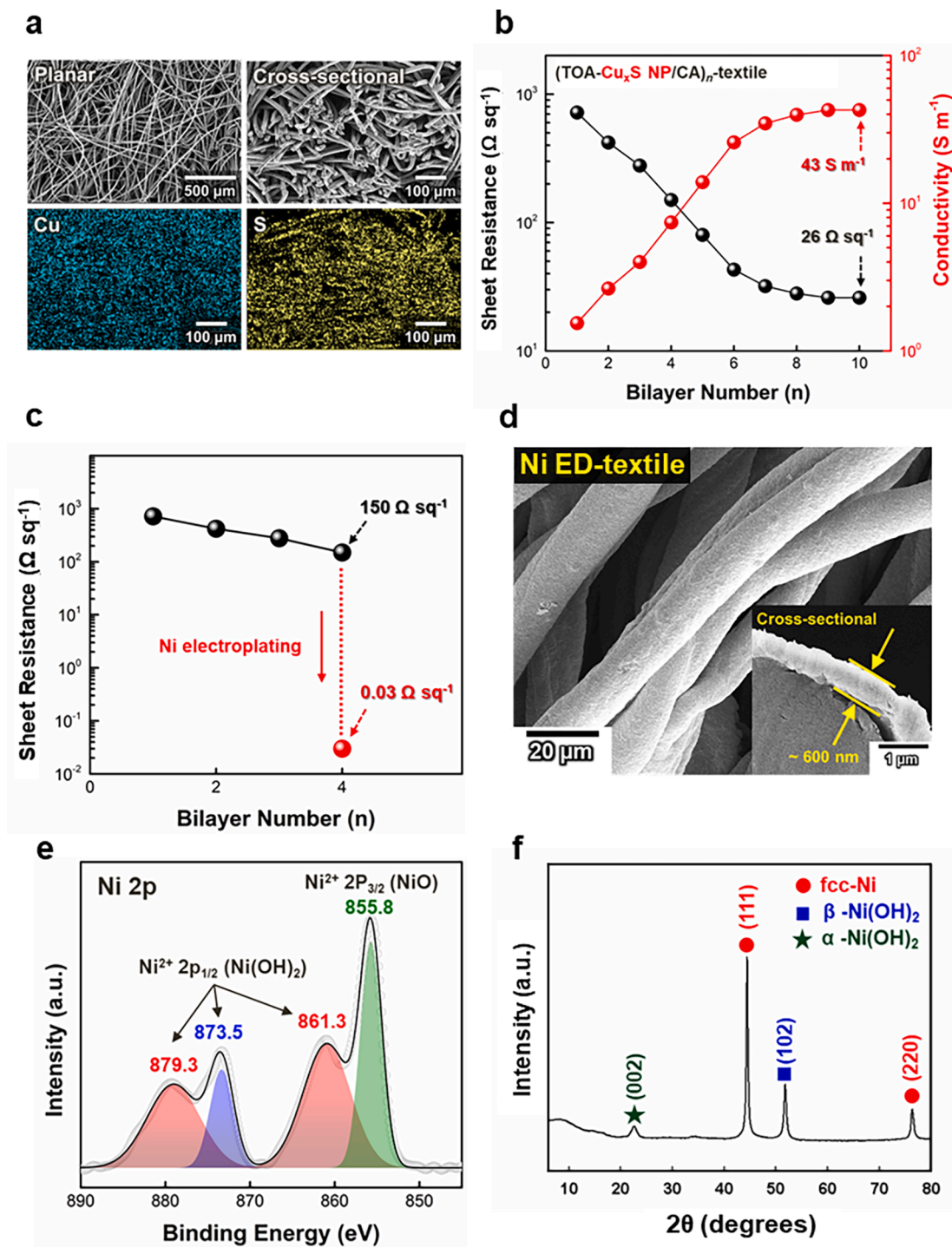

Fig. 4. (a) Planar/cross-sectional FE-SEM images, and corresponding EDS mapping images of the $(TOA-Cu_xS\ NP/CA)_{10}$-coated textiles. (b) Electrical properties of $(TOA-Cu_xS\ NP/CA)_n$-coated textiles with increasing bilayer number (n). (c) Sheet resistance before and after Ni-electrodeposition. (d) Planar FE-SEM images of the Ni ED-textile (the right inset shows the thickness of the Ni ED layer). (e) XPS spectra and (f) XRD data of Ni2p for the Ni ED-textile.

results, Ni electrodeposition was additionally performed onto the outermost CA-coated textile (i.e., (TOA-Cu$_x$S NP/CA)$_4$ multilayer-coated textiles) to prepare highly conductive TES electrodes. Notably, the 4 bilayer-coated textile possessed a sufficiently low sheet resistance (approximately 150 Ω sq^{-1}) suitable for Ni electrodeposition due to the formation of densely packed Cu$_x$S NP arrays. Specifically, when Ni was electrodeposited onto the (TOA-Cu$_x$S NP/CA)$_4$-coated textile in aqueous electrolyte solution, its sheet resistance sharply decreased from 150 to 0.03 Ω sq^{-1}, and additionally, the electrodeposited Ni metals were uniformly distributed within the textile (Fig. 4c and d). The specific surface areas of the bare textile and Ni ED-textile, which were measured using the mercury intrusion technique, were approximately 0.58 m^2 g^{-1} and 1.41 m^2 g^{-1}, respectively (Fig. S9). This increase in the specific surface of the Ni ED-textile can be attributed to the Ni protuberances created on the surface during electroplating (Fig. S10). The loading mass of electrodeposited Ni onto the conductive textile and the mass density of the resulting textile electrode were estimated to be approximately 36 mg cm^{-2} and 0.35 g cm^{-3}, respectively. These results evidently demonstrate that ultrathin JB LbL-assembled Cu$_x$S NP multilayers with controllable surface wettability (i.e., hydrophilic outermost NH$_2$ groups) can provide an effective pathway for conformal metal electrodeposition onto the respective fibrils within textiles. Although the conventional chemical reduction of Ni ions onto the bare textile could also generate the Ni textile, such a chemical reduction process induced a relatively high sheet resistance of ~3 Ω sq^{-1} (by the presence of organic impurities for chemical reduction) with a nonuniform and aggregated Ni structure (Fig. S11), which was in stark contrast to the Ni ED-textile prepared from our current approach.

Additionally, various mechanical tests showed that the Ni ED-textile, which was prepared from TOA-Cu$_x$S NP multilayer-induced electrodeposition, could maintain high electrical conductivity under repetitive external mechanical stimuli, such as bending (Fig. S12). Although the radius of the bending curvature was decreased up to 0.3 cm, the sheet resistance of the Ni ED-textile was preserved well without any meaningful change. Bending cycling tests of the Ni ED-textile were also performed with a bending curvature of ≈0.3 cm. Even after 5000 cycles, the sheet resistance of the Ni ED-textile was constantly maintained without any significant change, which was in stark contrast with that of the chemically reduced Ni textile. Adhesion property of (TOA-Cu$_x$S NP/CA)$_{10}$ on textile was also examined using the adhesive tape test (Fig. S13). After peeling off the adhesive tape attached to (TOA-Cu$_x$S NP/CA)$_{10}$-textile, a small amount of (TOA-Cu$_x$S NP/CA)$_{10}$-coated fibrils within the textile was peeled off in the form of fluff without the delamination of (TOA-Cu$_x$S NP/CA)$_{10}$ layer because of direct contact between the (TOA-Cu$_x$S NP/CA)$_{10}$-coated fibrils and the adhesive tape. In addition, we confirmed that there are no changes in the sheet resistance values of (TOA-Cu$_x$S NP/CA)$_{10}$-textile before and after peeling off test. Therefore, it is reasonable to conclude that the (TOA-Cu$_x$S NP/CA)$_{10}$ multilayers are deposited robustly on all fibrils within textile through Janus bond LbL-assembly leading to the high adhesion property.

Furthermore, the chemical and crystal structures of the Ni ED-textile were investigated using XPS and XRD analysis, respectively (Fig. 4e and f). First, in the XPS spectra of Ni *2p*, the observed peaks could be deconvoluted into two different kinds of nickel oxide peaks corresponding to Ni(OH)$_2$ (≈879.3, 873.5, and 861.3 eV) and NiO (≈855.8 eV). Additionally, the XRD pattern of the Ni ED-textile displayed strong (1 1 1) and (2 2 0) reflection peaks occurring from face-centered cubic (fcc) Ni. Furthermore, the (1 0 2) peak of β-Ni(OH)$_2$ with strong intensity and the (0 0 2) peak of α-Ni(OH)$_2$ with relatively low intensity were also observed from the Ni ED-textile.

Particularly, considering that nickel oxides such as α-Ni(OH)$_2$ and β-Ni(OH)$_2$ can act as pseudocapacitive components, these results suggested the possibility that the Ni ED-textile could be used as a pseudocapacitive textile as well as a conductive textile. Although α-Ni(OH)$_2$ has a higher specific capacitance than β-Ni(OH)$_2$, it should be noted that α-Ni(OH)$_2$ with a metastable structure is less electrochemically stable than β-Ni(OH)$_2$ with a thermodynamically stable phase structure [49,50]. On the other hand, the XRD spectrum of the chemically reduced Ni-textile exhibited a stronger peak intensity in α-Ni(OH)$_2$ than in β-Ni(OH)$_2$ (Fig. S14). These results implied that our Ni ED-textile could be effectively used as an energy storage electrode in alkaline media.

3.5. Electrochemical properties of the Ni electroplated textile electrodes

As mentioned above, considering that the presence of pseudocapacitive β-Ni(OH)$_2$ and the high electrical conductivity as well as the highly porous structure of the Ni ED-textile electrode are closely related to the pseudocapacitive performance, it is highly reasonable to analogize that the Ni ED-textile can have high energy storage performance (specifically areal capacitance, rate capability, and cycling stability). In view of energy storage materials, it is known that Ni(OH)$_2$ exhibits battery-like electrochemical properties with a Faradaic redox reaction, which displays clear redox peaks in cyclic voltammetry (CV) and voltage plateaus in the discharge profile [51,52]. This electrochemical reaction can be expressed as follows [53]:

$$Ni(OH)_2 + OH^- \leftrightarrow NiOOH + H_2O + e^- \tag{7}$$
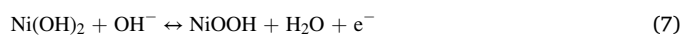
To specifically demonstrate the effectiveness of the Ni ED-textile, the CV of the Ni ED-textile was first measured in a 6 M KOH-based three-electrode system (Fig. 5a). When increasing the scan rate from 5 to 50 mVs^{-1} in a potential window ranging from 0.0 to 0.6 V (vs Hg/HgO), the Ni ED-textile exhibited a CV curve with a pair of evident redox peaks occurring from the reversible Faradaic reaction, which implied the typical pseudocapacitive (or battery-like) behavior of the Ni ED layer.

Furthermore, the Ni ED-textile exhibited 88.6 % capacitance retention after the cycling stability test of 10,000 cycles (at a scan rate of 20 mV s^{-1}) while preserving the surface structural morphology without cracking and/or delamination of the Ni layer (Fig. 5b and Fig. S15). The galvanostatic charge–discharge (GCD) profiles for the Ni ED-textile were measured to investigate the charge storage capabilities at a variety of current densities ranging from 3 to 32 mA cm^{-2} (Fig. 5c). The GCD curves also displayed a voltage plateau originating from the Faradaic redox reaction of Ni(OH)$_2$, which corresponded to the results from the CV curves of Fig. 5a. Particularly, it should be noted that the Ni ED-textile itself could exhibit a high areal capacitance despite the electrodeposition of only the Ni layer without any additional pseudocapacitive component. Based on these GCD results, the areal capacitance and specific capacitance of the Ni ED-textile were evaluated to be 2.56 F cm^{-2} and 723 F g^{-1} (at 3 mA cm^{-2}), respectively, with a high coulombic efficiency of 98.3 % (at 32 mA cm^{-2}) (Fig. 5d, Experimental Sections, and Table S1). Additionally, the Ni ED-textile maintained 72.5 % of its initial capacitance after 5,000 cycles of GCD measurement at a current density of 32 mA cm^{-2} (Fig. S16). The areal capacitance of 2.56 F cm^{-2} shown in our approach was considerably high compared to commercial Ni foam with almost negligible areal capacity values (<0.05 F cm^{-2}) (Fig. S17), which was mainly due to the large active surface area with a highly uniform fibril structure of the Ni ED-textile, including Ni(OH)$_2$. Furthermore, it is worth noting that the Ni ED-textile exhibits a higher or comparable areal capacitance to previously reported textile-based electrodes (Table S1).

To further investigate the electrochemical behavior of the Ni ED-textile electrode, electrochemical impedance spectroscopy (EIS) measurements were additionally performed in the frequency range from 10^5 to 0.1 Hz (Fig. S18). In this case, the Ni ED-textile electrode revealed a relatively low equivalent series resistance (R_s) of 0.81 Ω cm^2. Additionally, only a slight change in the R_s value (from 0.81 to 1.09 Ω cm^2) and Warburg impedance of the Ni ED-textile were observed after 10,000 cycles. It should be noted that these good electrochemical performances of Ni ED-textile electrodes could be realized by both the high electrical conductivity of the Ni ED layer and the highly uniform pseudocapacitive
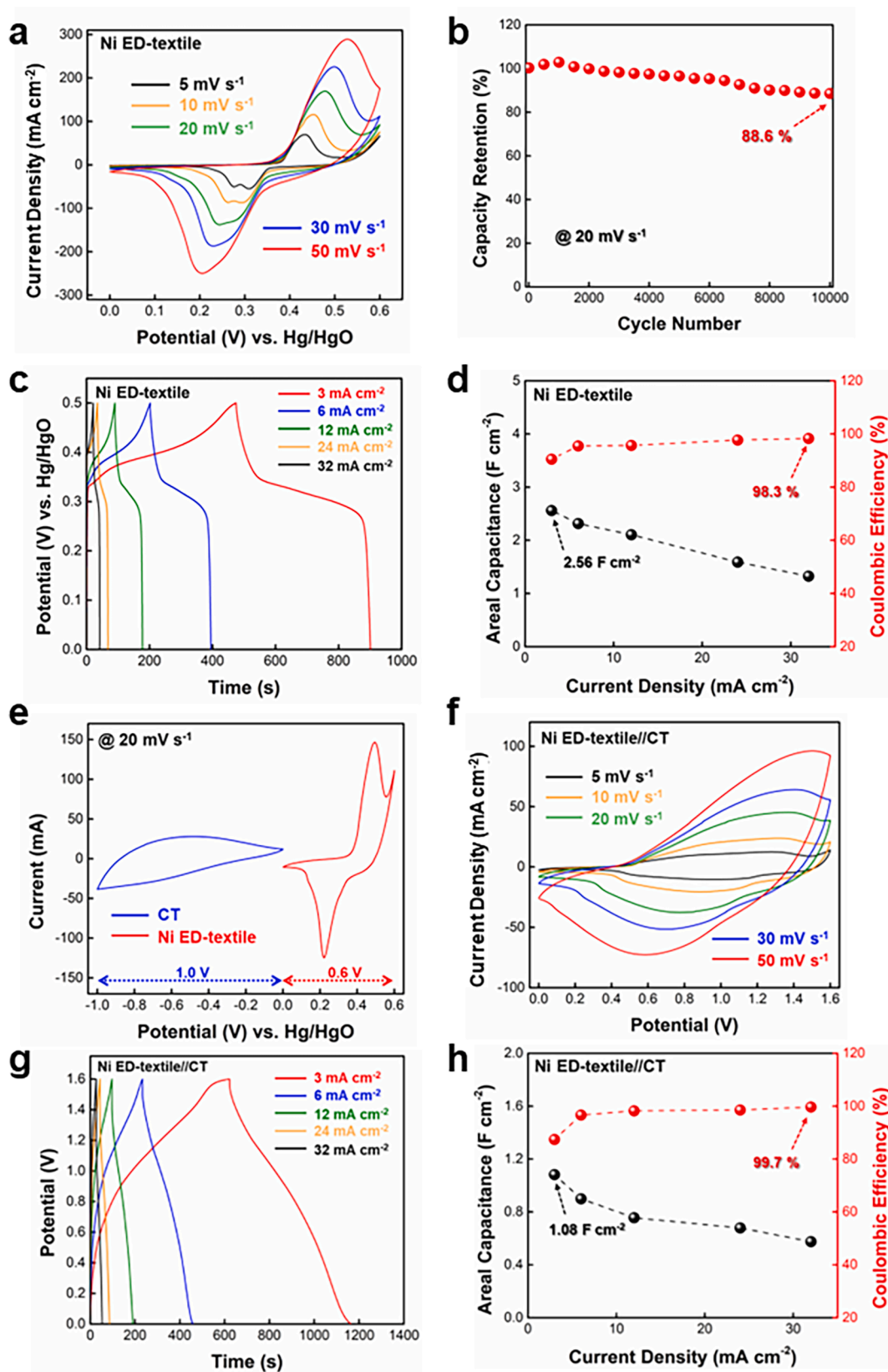
Fig. 5. (a) CV curves of the Ni ED-textile electrodes at various scan rates from 5 to 50 mV s^{-1} in a three-electrode system. (b) Electrochemical cycling stability of the Ni ED-textile electrodes under 10,000 cycles of CV at 20 mV s^{-1}. (c) GCD profiles of the Ni ED-textile electrodes at current densities from 3 to 32 mA cm^{-2}. (d) Areal capacitance and Coulombic efficiency of the Ni ED-textile electrodes as a function of current density. (e) CV curves of the Ni ED-textile and CT at a scan rate of 20 mV s^{-1}. (f) CV curve of the full-cell (Ni ED-textile//CT) at scan rates from 5 to 50 mVs^{-1}. (g) GCD profiles of the full-cell electrode measured at current densities from 3 to 32 mA cm^{-2}. (h) Areal capacitance and Coulombic efficiency of the full-cell electrode as a function of current density.

structure that were formed by favorable interfacial interactions between the Ni ED layer and the CA-capped Cu$_x$S NP multilayers as well as between the CA-capped Cu$_x$S NP multilayers and the cotton textile. As a result, the electrical, electrochemical, and structural characteristics of the Ni ED-textile could induce high energy storage performance.

Based on these results, we also prepared asymmetric full-cell pseudocapacitors composed of a Ni ED-textile cathode and the corresponding textile anode. For this goal, a carbonized textile (CT) with a sheet resistance of approximately 10 Ω sq^{-1} and a highly porous structure was used as an anode to meet the high electrochemical performance of the Ni ED-textile cathode. In this case, the CV curves of the CT anode with a broad oxidation peak at various scan rates indicated that the charge storage mechanism of the CT anode was mainly caused by the electrical double layered capacitance (EDLC) and reversible faradaic reaction (Fig. S19a). The areal capacitance of CT was measured to be approximately 1.35 F cm^{-2} at a current density of 3 mA cm^{-2} (Fig. S19b). Considering the charge balance (q$^+$ = q$^-$) of each electrode, the area of the CT anode was almost similar to that of the Ni ED-textile cathode to prepare the full-cell electrodes (i.e., Ni ED-textile//CT). In line with these charge balances and CV curves, the Ni ED-textile and CT exhibited stable electrochemical behavior in the potential range of 0 to 0.6 V and -1.0 to 0 V, respectively (Fig. 5e). Based on these results, the potential window of the full-cell electrodes could be extended up to 1.6 V in 6 M KOH solution. Additionally, the CV curves of the full-cell electrodes observed from different operation voltage windows ranging from 0.6 to 1.6 V at a scan rate of 50 mV s^{-1} showed a stable pseudocapacitive characteristic with a reversible Faradaic reaction (Fig. S20). The CV curves of full-cell electrodes also exhibited both EDLC and pseudocapacitive characteristics at various scan rates from 5 to 50 mV s^{-1} (Fig. 5f). Additionally, quasi-triangular symmetric GCD profiles from 3 to 32 mA cm^{-2} also supported that the full-cell electrodes had desirable pseudocapacitive features and good rate capabilities (Fig. 5g). In particular, these electrodes exhibited high areal capacitances of approximately 1.08 F cm^{-2} at a current density of 3 mA cm^{-2} and delivered an excellent Coulombic efficiency of 99.7 % at a current density of 32 mA cm^{-2} (Fig. 5h). Additionally, the areal (volumetric) energy densities of our devices were calculated to be approximately 0.34 mW h cm^{-2} (3.30 mW h cm^{-3}) at a power density of 2.25 mW cm^{-2} (21.8 mW cm^{-3}) and 0.18 mW h cm^{-2} (1.75 mW h cm^{-3}) at a power density of 24 mW cm^{-2} (233 mW cm^{-3}). These results evidently demonstrated that our approach using JB LbL assembly and subsequent Ni electrodeposition could be effectively applied to textile-based energy storage applications with high performance.

4. Conclusion

In this study, we demonstrated a robust and efficient strategy for the preparation of a textile-based pseudocapacitive electrode allowing for a highly porous structure, excellent electrical conductivity, stable mechanical flexibility, good rate capability, and high areal capacitance. The key feature of our approach is that the synthesized TOA-Cu$_x$S NPs can be densely assembled with CA molecular ligands onto the cotton textile using JB LbL assembly, which can further induce the electrodeposition (i.e., Ni electroplating) onto the Cu$_x$S NP-based conductive textile with controllable surface wettability. Owing to these favorable interfacial interactions between cotton textile and Cu$_x$S NP arrays as well as between electroplated Ni and Cu$_x$S NP arrays, the initially insulating cotton textiles could be completely converted to high-performance pseudocapacitive textile electrodes with an all-in-one fibril structure, which was in stark contrast with conventional textile electrodes with a nonuniform and aggregated fibril structure. The formed Ni ED-textile exhibited a high areal capacitance of 2.56 F cm^{-2} (at 3 mA cm^{-2}), good rate capability, and high cycling stability. When Ni ED-textile and carbonized cotton textile were used as the cathode and anode, respectively, the resulting full-cell electrodes also exhibited a high areal capacitance of 1.08 F cm^{-2} (at 3 mA cm^{-2}) and good rate

capability. We believe that our approach using JB LbL assembly and Ni electrodeposition can open up new possibilities in developing and designing advanced textile-based energy storage electrodes.

Declaration of Competing Interest

The authors declare that they have no known competing financial interests or personal relationships that could have appeared to influence the work reported in this paper.

Data availability

The authors do not have permission to share data.

Appendix A. Supplementary data

Supplementary data to this article can be found online at https://doi.org/10.1016/j.cej.2022.140150.

References

[1] J.R. Miller, P. Simon, Electrochemical capacitors for energy management, Science 321 (2008) 651.
[2] M. Armand, J.M. Tarascon, Building better batteries, Nature 451 (2008) 652.
[3] J. Ji, Y. Li, W. Peng, G. Zhang, F. Zhang, X. Fan, Advanced graphene-based binder-free electrodes for high-performance energy storage, Adv. Mater. 27 (2015) 5264.
[4] Y. Shao, M.F. El-Kady, J. Sun, Y. Li, Q. Zhang, M. Zhu, H. Wang, B. Dunn, R.B. Kaner, Design and mechanisms of asymmetric supercapacitors, Chem. Rev. 118 (2018) 9233.
[5] C. Choi, D.S. Ashby, D.M. Butts, R.H. DeBlock, Q. Wei, J. Lau, B. Dunn, Achieving high energy density and high power density with pseudocapacitive materials, Nat. Rev. Mater. 5 (2020) 5.
[6] Z. Song, W. Li, Y. Bao, Z. Sun, L. Gao, M.H. Nawaz, D. Han, L. Niu, A new route to tailor high mass loading all-solid-state supercapacitor with ultra-high volumetric energy density, Carbon 136 (2018) 46.
[7] Z. Zhang, H. Huo, L. Wang, S. Lou, L. Xiang, B. Xie, Q. Wang, Stacking fault disorder induced by Mn doping in Ni(OH)$_2$ for supercapacitor electrodes, Chem. Eng. J. 412 (2021), 128617.
[8] Z. Song, Y. Fan, Z. Sun, D. Han, Y. Bao, L. Niu, A new strategy for integrating superior mechanical performance and high volumetric energy density into a Janus graphene film for wearable solid-state supercapacitors, J. Mater. Chem. A 5 (2017) 20797.
[9] Q. Huang, D. Wang, Z. Zheng, Textile-based electrochemical energy storage devices, Adv. Energy Mater. 6 (2016) 1600783.
[10] Y. Ko, M. Kwon, W.K. Bae, B. Lee, S.W. Lee, J. Cho, Flexible supercapacitor electrodes based on real metal-like cellulose papers, Nat. Commun. 8 (2017) 536.
[11] K. Jost, C.R. Perez, J.K. McDonough, V. Presser, M. Heon, G. Dion, Y. Gogotsi, Carbon coated textiles for flexible energy storage, Energy Environ. Sci. 4 (2011) 5060.
[12] Y. Wang, X. Hong, Y. Guo, Y. Zhao, X. Liao, X. Liu, Q. Li, L. He, L. Mai, Wearable textile-based Co−Zn alkaline microbattery with high energy density and excellent reliability, Small 16 (2020) 2000293.
[13] M. Kwon, D. Nam, S. Lee, Y. Kim, B. Yeom, J.H. Moon, S.W. Lee, Y. Ko, J. Cho, Textile-type lithium-ion battery cathode enabling high specific/areal capacities and high rate capability through ligand replacement reaction-mediated assembly, Adv. Energy Mater. 11 (2021) 2101631.
[14] P. Sun, M. Qiu, M. Li, W. Mai, G. Cui, Y. Tong, Stretchable Ni@NiCoP textile for wearable energy storage clothes, Nano Energy 55 (2019) 506.
[15] Q. Li, J. Wang, C. Liu, S.M. Fakhrhoseini, D. Liu, L. Zhang, W. Lei, M. Naebe, Controlled design of a robust hierarchically porous and hollow carbon fiber textile for high-performance freestanding electrodes, Adv. Sci. 6 (2019) 1900762.
[16] S.Y. Cho, Y.S. Yun, S. Lee, D. Jang, K.-Y. Park, J.K. Kim, B.H. Kim, K. Kang, D.L. Kaplan, H.J. Jin, Carbonization of a stable β-sheet-rich silk protein into a pseudographitic pyroprotein, Nat. Commun. 6 (2015) 7145.
[17] A. Sahasrabudhe, H. Dixit, R. Majee, S. Bhattacharyya, Value added transformation of ubiquitous substrates into highly efficient and flexible electrodes for water splitting, Nat. Commun. 9 (2018) 2014.
[18] L. Liu, Y. Yu, C. Yan, K. Li, Z. Zheng, Wearable energy-dense and power-dense supercapacitor yarns enabled by scalable graphene–metallic textile composite electrodes, Nat. Commun. 6 (2015) 7260.

[19] T. Zhang, X. Li, E. Asher, S. Deng, X. Sun, J. Yang, Paper with Power: Engraving 2D materials on 3D structures for printed, high-performance, binder-free, and all-solid-state supercapacitors, Adv. Funct. Mater. 28 (2018) 1803600.

[20] H.-J. Hwang, K.-H. Oh, H.-S. Kim, All-photonic drying and sintering process via flash white light combined with deep-UV and near-infrared irradiation for highly conductive copper nano-ink, Sci. Rep. 6 (2016) 19696.

[21] M. Zou, W. Zhao, H. Wu, H. Zhang, W. Xu, L. Yang, S. Wu, Y. Wang, Y. Chen, L. Xu, A. Cao, Single carbon fibers with a macroscopic-thickness, 3D highly porous carbon nanotube coating, Adv. Mater. 30 (2018) 1704419.

[22] X. Liang, H. Li, J. Dou, Q. Wang, W. He, C. Wang, D. Li, J.-M. Lin, Y. Zhang, Stable and biocompatible carbon nanotube ink mediated by silk protein for printed electronics, Adv. Mater. 32 (2020) 2000165.

[23] L.V. Thekkekara, M. Gu, Large-scale waterproof and stretchable textile-integrated laser- printed graphene energy storages, Sci. Rep. 9 (2019) 11822.

[24] B. Dudem, A.R. Mule, H.R. Patnam, J.S. Yu, Wearable and durable triboelectric nanogenerators via polyaniline coated cotton textiles as a movement sensor and self-powered system, Nano Energy 55 (2019) 305.

[25] H. Zhao, L. Liu, R. Vellacheri, Y. Lei, Recent advances in designing and fabricating self-supported nanoelectrodes for supercapacitors, Adv. Sci. 4 (2017) 1700188.

[26] Y. Gao, C. Xie, Z. Zheng, Textile composite electrodes for flexible batteries and supercapacitors: opportunities and challenges, Adv. Energy Mater. 11 (3) (2021) 2002838.

[27] H. Sun, S. Xie, Y. Li, Y. Jiang, X. Sun, B. Wang, H. Peng, Large-area supercapacitor textiles with novel hierarchical conducting structures, Adv. Mater. 28 (2016) 8431.

[28] K. Jost, D. Stenger, C.R. Perez, J.K. McDonough, K. Lian, Y. Gogotsi, G. Dion, Knitted and screen printed carbon-fiber supercapacitors for applications in wearable electronics, Energy Environ. Sci. 6 (2013) 2698.

[29] C.H. Kwon, M. Kang, M. Kwon, D. Nam, Y. Song, E. Yong, M.-K. Oh, Y. Kim, B. Yeom, J.H. Moon, S.W. Lee, J. Cho, High-performance hybrid biofuel cells using amphiphilic assembly-based enzyme electrodes, Appl. Phys. Rev. 9 (2022), 021413.

[30] W. Chang, D. Nam, S. Lee, Y. Ko, C.H. Kwon, Y. Ko, J. Cho, Fibril-Type Textile Electrodes Enabling Extremely High Areal Capacity through Pseudocapacitive Electroplating onto Chalcogenide Nanoparticle-Encapsulated Fibrils, Adv. Sci. 2203800 (2022).

[31] O.P. Watts, Rapid nickel plating, Trans. Am. Electrochem. Soc. 29 (1916) 395.

[32] V. Khomenko, E. Raymundo-Piñero, F. Béguin, Optimisation of an asymmetric manganese oxide/activated carbon capacitor working at 2 V in aqueous medium, J. Power Sources 153 (2006) 183.

[33] D.A. Buttry, Advances in electroanalytical chemistry: applications of the QCM to electrochemistry, Marcel Dekker, New York, 1991.

[34] S. Zhang, N. Pan, Supercapacitors performance evaluation, Adv. Energy Mater. 5 (2015) 1401401.

[35] X. Dai, D. Chen, H. Fan, Y. Zhong, L. Chang, H. Shao, J. Wang, J. Zhang, C. Cao, Ni (OH)$_2$/NiO/Ni composite nanotube arrays for high-performance supercapacitors, Electrochim. Acta 154 (2015) 128.

[36] Y. Zhao, H. Pan, Y. Lou, X. Qiu, J.J. Zhu, C. Burda, Plasmonic Cu$_{2-x}$S nanocrystals: optical and structural properties of copper-deficient copper(I) sulfides, J. Am. Chem. Soc. 131 (2009) 4253.

[37] K.S. Murasheva, S.V. Saikova, S.A. Vorobiev, A.S. Romanchenko, Y.L. Mikhlin, Characteristics of copper sulfide nanoparticles obtained in the copper sulfate–sodium thiosulfate system, J. Struct. Chem. 58 (2017) 1383.

[38] J. Cho, K. Char, Effect of layer integrity of spin self-assembled multilayer films on surface wettability, Langmuir 20 (2004) 4011.

[39] W. Maketon, K.L. Ogden, Synergistic effects of citric acid and polyethylenimine to remove copper from aqueous solutions, Chemoshpere 75 (2009) 206.

[40] J. Lakshmipraba, S. Arunachalama, D. Avinash, G. Thyagarajan, T. Thirunalasundarib, Synthesis, nucleic acid binding and cytotoxicity of polyethyleneimine-copper(II) complexes containing 1,10-phenanthroline and L-valine, Eur. J. Med. Chem. 46 (2011) 3013.

[41] A.J. Nozik, M.C. Beard, J.M. Luther, M. Law, R.J. Ellingson, J.C. Johnson, Semiconductor quantum dots and quantum dot arrays and applications of multiple exciton generation to third-generation photovoltaic solar cells, Chem. Rev. 110 (2010) 6873.

[42] W. Aigner, G.K. Nenova, M.A. Sliem, R.A. Fischer, M. Stutzmann, R.N. Pereira, Electronic changes induced by surface modification of Cu$_{2-x}$S Nanocrystals, J. Phys. Chem. C 119 (2015) 16276.

[43] M.Z. Ansari, N. Khare, Thermally activated band conduction and variable range hopping conduction in Cu$_2$ZnSnS$_4$ thin films, J. Appl. Phys. 117 (2015), 025706.

[44] E.R. Viana, J.C. González, G.M. Ribeiro, A.G.d. Oliveira, 3D hopping conduction in SnO$_2$ nanobelts, Phys. Status Solidi RRL 6 (6) (2012) 262–264.

[45] G.D.M.R. Dabera, M. Walker, A.M. Sanchez, H.J. Pereira, R. Beanland, R.A. Hatton, Retarding oxidation of copper nanoparticles without electrical isolation and the size dependence of work function, Nat. Commun. 8 (2017) 1894.

[46] C. Barrière, K. Piettre, V. Latour, O. Margeat, C.-O. Turrin, B. Chaudret, P. Fau, Ligand effects on the air stability of copper nanoparticles obtained from organometallic synthesis, J. Mater. Chem. 22 (2012) 2279.

[47] K.P. Rice, E.J. Walker, J.M.P. Stoykovich, A.E. Saunders, Solvent-dependent surface plasmon response and oxidation of copper nanocrystals, J. Phys. Chem. C 115 (2011) 1793.

[48] M. Yin, C.-K. Wu, Y. Lou, C. Burda, J.T. Koberstein, Y. Zhu, S. O'Brien, Copper oxide nanocrystals, J. Am. Chem. Soc. 127 (2005) 9506.

[49] T.A. Han, J.P. Tu, J.B. Wu, Y. Li, Y.F. Yuan, Electrochemical properties of biphase Ni(OH)$_2$ electrodes for secondary rechargeable Ni/MH batteries, J. Electrochem. Soc. 153 (2006) A738.

[50] U.M. Patil, K.V. Gurav, V.J. Fulari, C.D. Lokhande, O.S. Joo, Characterization of honeycomb-like "β-Ni(OH)$_2$" thin films synthesized by chemical bath deposition method and their supercapacitor application, J. Power Sources 188 (2009) 338.

[51] P. Simon, Y. Gogotsi, B. Dunn, Where do batteries end and supercapacitors begin? Science 343 (2014) 1210.

[52] T. Brousse, D. Bélanger, J.W. Long, To be or not to be pseudocapacitive? J. Electrochem. Soc. 162 (2015) A5185.

[53] C.Y. Wang, S. Zhong, K. Konstantinov, G. Walter, H.K. Liu, Structural study of Al-substituted nickel hydroxide, Solid State Ion. 148 (2002) 503.